ACS APPLIED MATERIALS & INTERFACES

Research Article

www.acsami.org

High-Efficiency Aqueous-Processed Hybrid Solar Cells with an Enormous Herschel Infrared Contribution

Gan Jin,[†] Hao-Tong Wei,[‡] Tian-Yi Na,[‡] Hai-Zhu Sun,*[,†] Hao Zhang,[‡] and Bai Yang*[,‡]

[†]College of Chemistry, Northeast Normal University, Changchun 130024, Jilin, People's Republic of China

[‡]State Key Laboratory of Supramolecular Structure and Materials, College of Chemistry, Jilin University, Changchun 130012, Jilin, People's Republic of China

Supporting Information

ABSTRACT: Aqueous-processed solar cells have evolved into a new generation of promising and renewable energy materials due to their excellent optical, electrical, and low-cost properties. In this work, $Cd_{0.75}Hg_{0.25}Te$ colloid quantum dots (CQDs) were incorporated into a water-soluble conjugated polymer with broad absorption and high charge-carrier-mobility (5×10^{-4} cm^2 V^{-1} s^{-1}) to obtain a composite with an absorption spectrum ranging from 300 to 1200 nm. The matched energy level between polymer and CQDs ensured the effective electron transfer, while the interpenetrating network structure formed via heat treatment guaranteed the quick electron transport. Moreover, the formation process of the interpenetrating network was systematically monitored by using AFM and TEM instruments and further confirmed through the measurement of charge-carrier-mobility of the active layers. In combination with the surface modification of a single $Cd_{0.75}Hg_{0.25}Te$ layer, this aqueous-processed solar cell showed excellent photovoltaic response and the power conversion efficiency (PCE) reached 2.7% under AM 1.5 G illumination (100 mW cm^{-2}). Especially, the contribution of the Herschel infrared region (780–1100 nm) to the photocurrent was as high as 15.04%. This device showed the highest PCE among organic-inorganic hybrid solar cells (HSCs) based on $Cd_xHg_{1-x}Te$ CQDs and the highest near infrared (NIR) contribution among aqueous-processed HSCs, indicating the enormous potential of taking advantage of NIR energy in a solar spectrum and a promising application in solar cells especially used in cloudy weather.

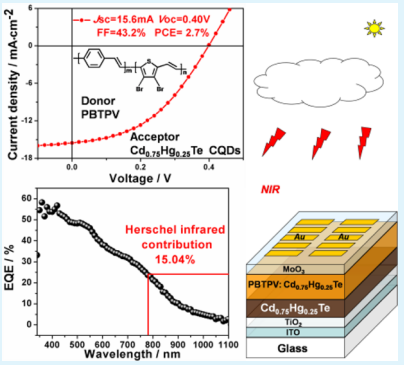

KEYWORDS: *aqueous-processed, hybrid solar cells, colloidal quantum dots, near infrared*

1. INTRODUCTION

Recently, people have turned a great deal of attention to the renewable energy source, especially to the solar cells because of more and more severe ecological and environmental issues.[1−5] Different photovoltaic devices have been fabricated to obtain solar cells with high performance by employing different materials. One basic principle is to enlarge the absorption of devices to the solar energy. Therefore, people are designing tandem solar cells with different absorption materials or low band-gap materials to match the solar spectrum.[6−13] In addition, the desired solar cells should adapt to different weather conditions due to inhomogeneous territory on the Earth and practical industrial applications in the near future. For example, many regions face a perennial cloudy weather, and the design of solar cells possessing near infrared (NIR) absorption is highly appraisable because NIR ray can penetrate the dense cloud layers. What is more, half of the sun's power reaching the surface of the Earth belongs to the infrared.[14] Consequently, it is significant to develop a high efficient, low-cost, and low toxic approach to fabricate solar cells with high NIR contribution.

Being an important member of the solar cells, organic-inorganic hybrid solar cells (HSCs) based on conjugated polymer/colloidal quantum dots (CQDs) have evolved into a new generation of promising and renewable energy material. This kind of solar cell has the advantages of low cost of the polymer materials and high charge mobility of inorganic semiconductor CQDs.[15−25] Recently, Ma and co-workers have gotten an infusive achievement that they fabricated a sort of photovoltaic device consisting of conjugated polymer and PbS_xSe_{1-x} CQDs with the highest power conversion efficiency (PCE) of 5.50% among the HSCs through the oil phase method.[26] Considering the green chemistry concept,[27−30] the aqueous-processed HSCs possess the advantages of environmentally-friendly, low cost, and low toxicity. In our previous work, we firstly fabricated aqueous-processed HSCs employing poly(*p*-phenylene-vinylene) (PPV) and CdTe CQDs with a PCE of 2.14%,[31] which was comparable to the HSCs processed from an oily phase approach. However, this aqueous-processed solar cell has an inferior absorption beyond visible light due to the limited absorption by CQDs, that is to say, cloudy weather would immensely decrease their performance. Alternatively, $Cd_xHg_{1-x}Te$ is one of the most important mercury compounds due to the wide range of tunable optical and electrical

Received: March 11, 2014
Accepted: May 8, 2014
Published: May 8, 2014

properties, obtained through compositional tuning (x) of this material.[32] Considering that $Cd_xHg_{1-x}Te$ CQDs have broad absorption in the NIR region, the HSCs consisting of PPV and $Cd_{0.75}Hg_{0.25}Te$ CQDs were developed, but the PCE was only 1.5%,[33] which was determined by the narrow absorption region (300−550 nm) and low charge-carrier-mobility (1.1×10^{-4} cm^2 V^{-1} s^{-1}) of PPV. Moreover, only one extremely thin $Cd_{0.75}Hg_{0.25}Te$ layer determined its limited absorption within NIR region. Therefore, it is still a challenge to prepare high performance HSCs with high NIR absorption by using an aqueous-processed approach.

Herein, we introduced water-soluble conjugated polymer poly[(3,4-dibromo-2,5-thienylene-vinylene)-*co*-(*p*-phenylene-vinylene)] (PBTPV) with broad absorption (300−700 nm) and high charge-carrier-mobility (5×10^{-4} cm^2 V^{-1} s^{-1})[34] into the HSCs. Combined with the interfacial modification by $Cd_{0.75}Hg_{0.25}Te$ CQDs, the obtained solar cells of PBTPV:$Cd_{0.75}Hg_{0.25}Te$ showed a satisfactory photovoltaic response with a PCE of 2.7% under AM 1.5G illumination (100 mW cm^{-2}), 80% higher than that of the PPV:$Cd_{0.75}Hg_{0.25}Te$ solar cells. Especially, the solar cells presented at least 15.04% NIR contribution, which was 32% higher than that of the PPV:$Cd_{0.75}Hg_{0.25}Te$ solar cells. To our knowledge, this PCE is the highest value for the NIR HSCs fabricated via an aqueous-processed approach.

2. EXPERIMENTAL SECTION

2.1. Materials. Tellurium powder (200 mesh, 99.8%), R,R0-dichloro-*p*-xylene (98%), tetrahydrothiophene (99%), and 3-mercaptopropionic acid (MPA) were all purchased from Aldrich Chemical Crop. Paraformaldehyde (96+%) and 2-mercaptoethylaminehydrochloride (2-MA, 98%) was obtained from Acros. 3,4-Dibromothiophene was purchased from Aladdin. $ZnCl_2$ (98+%), $CdCl_2$ (99+%), $HgCl_2$ (99+%), and tetrabutyltitanate and sodium borohydride ($NaBH_4$, 99%) were commercially available. All of the solvents were analytical grade and used as received.

2.2. Preparation of Aqueous $Cd_{0.75}Hg_{0.25}Te$ CQDs. The $Cd_{0.75}Hg_{0.25}Te$ CQDs were prepared according to the following method. Freshly prepared NaHTe solution was added into a N_2-saturated aqueous solution of $CdCl_2$ and $HgCl_2$ at pH 9 in the presence of MPA as a stabilizing agent. The ratio of metal ions:MPA:HTe^- was 1:2.9:0.5, and the concentration of metal ion was 3.75×10^{-3} M. The ratio of Cd^{2+} to Hg^{2+} was 3. The solution was then placed in an oven at 40 °C for 30 min and finally preserved in a dark place.

2.3. Preparation of PBTPV Precursor and PBTPV. Chloromethylation and Wessling polymerization dominated the primary synthesis of PBTPV as shown in Scheme 1. The details of the synthetic method were described as follows: a stream of dry hydrogen chloride was added into a stirred solution consisting of 0.5 g of $ZnCl_2$, 1.25 g of paraformaldehyde, and 2.5 mL of concentrated HCl acid, allowing the temperature to rise to 50−60 °C. Until the solution was saturated with HCl, 3 mL of 3,4-dibromothiophene was added dropwise with stirring, and the mixture was stirred for 6 h. Then, the oily lower layer of the mixture was siphoned off and washed with cold water for several times. The oil was filtered to remove the residual paraformaldehyde, and then 30 mL of methanol was added, followed by 2.6 mL of tetrahydrothiophene. This solution was kept at 50 °C for 24 h to convert the 2,5-dichloromethyl-3,4-dibromothiophene to the sulfonium salt monomer (M_1). The *p*-xylylenebis(tetrahydrothiophenium chloride) (M_2) was prepared using the reaction between *p*-xylylene dichloride and tetrahydrothiophene at 50 °C for 24 h in a 1:2 molar ratio. Then, 10 mL of 0.4 M NaOH was added into a highly cold mixed solution composed of 1.24 g M_1, 0.56 g M_2, and 10 mL of methanol with moderate stirring. The reaction proceeded for 1 h and was terminated by addition of 0.4 M HCl aqueous solution to neutralize the surplus alkali. The whole process was carried out at 0−5 °C under nitrogen. Finally, the mixture was collected, and the impure aqueous solution of the PBTPV precursor was dialyzed against deionized water for 1 week to remove some small molecules. The PBTPV precursor can be heat transferred into PBTPV at 300 °C for 1 h under the protection of N_2.

Scheme 1. Preparation Process of the Water-Soluble Conjugated Polymer PBTPV

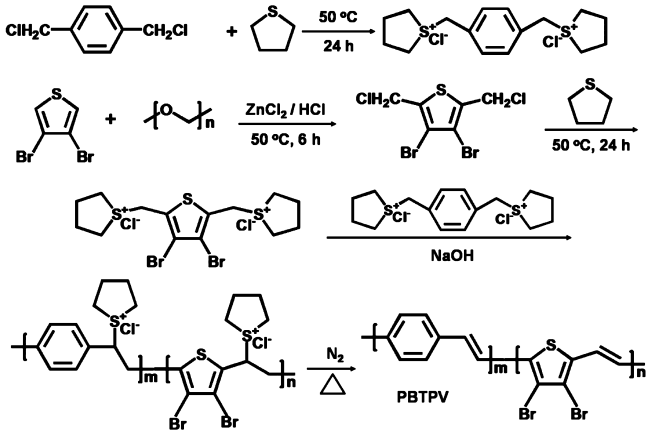

2.4. Preparation of TiO_2 Precursor. In a typical synthesis, 4 mL of tetrabutyltitanate was dissolved in 2 mL of isopropyl alcohol in a conical flask for 5 min. 210 μL of water and 17 μL of concentrated HCl were mixed with 4 mL of isopropyl alcohol for 5 min. Then, this solution was dropped into the conical flask over about 10 min, and the mixture was stirred for 12 h at room temperature. Before use, the resultant TiO_2 precursor was diluted with isopropyl alcohol.

2.5. Device Fabrication. ITO-coated glasses first underwent ultrasonic treatment in chloroform, acetone, isopropyl, and then were rinsed by deionized water before drying in N_2 flow, followed by the oxygen plasma treatment for 5 min. Then spin-coating of the TiO_2 layer (about 30 nm) at 2000 r per min (rpm) for 10 s, followed by annealing at 350 °C for 15 min under N_2 to convert the TiO_2 precursor into anatase-phase TiO_2. Before spin-coating of the $Cd_{0.75}Hg_{0.25}Te$ CQDs or the blending of the donor and acceptor, the $Cd_{0.75}Hg_{0.25}Te$ CQDs underwent ligand exchange with a concentration of 2 g mL^{-1} 2-MA water solution, and the precipitate was obtained by centrifugation at 8000 rpm for 2 min. The precipitated $Cd_{0.75}Hg_{0.25}Te$ CQDs were redissolved in 2-MA water solution and further centrifugated by addition of isopropyl alcohol to remove the superfluous salts and ligands, and this process was repeated two times. The precipitated CQDs were redissolved in deionized water with a concentration of 84 mg mL^{-1}. The $Cd_{0.75}Hg_{0.25}Te$ layer (about 40 nm) was prepared by a spin-coating process with a revolving speed of 800 rpm followed by a 10 min of annealing at 300 °C. Next, the photoactive layer (about 80 nm) was formed by spin-coating (at 800 rpm), with an aqueous solution containing 1.67 mg mL^{-1} PBTPV precursor and 56 mg mL^{-1} $Cd_{0.75}Hg_{0.25}Te$ CQDs. The blend film was annealed at 300 °C in a glove box for 1 h. Finally, a 4 nm thick MoO_3 layer and Au electrodes with 80 nm thickness were evaporated on the photoactive layer sequentially with a 4.5 mm^2 mask.

2.6. Characterization. UV-vis spectra were acquired on a Shimadzu 3600 UV-vis-NIR spectrophotometer. Fluorescence spectra were acquired on a Shimadzu RF-5301 PC spectrofluorimeter, and the excitation wavelength was 365 nm. Atomic force microscopy (AFM) images were recorded in tapping mode with a Digital Instruments NanoScopeIIIa under ambient conditions. Transmission electron microscopy (TEM) images were recorded on a JEOL-2010 electron microscope operating at 200 kV. The film thicknesses were measured on an Ambios Tech. XP-2 profilometer. The current density-voltage (*J*−*V*) characterization of PV devices under white-light illumination from an SCIENCETECH 500-W solar simulator (AM 1.5G, 100 mW cm^{-2}) was carried out on computer-controlled Keithley 2400 Source Meter measurement system in a glove box filled with nitrogen

dx.doi.org/10.1021/am501408v | ACS Appl. Mater. Interfaces 2014, 6, 8606−8612

atmosphere (<1 ppm of H_2O and <1 ppm of O_2). EQE was measured under illumination of monochromatic light from the xenon lamp using a monochromator (JobinYvon, TRIAX 320) and detected by a computer-controlled Stanford SR830 lock-in amplifier with a Stanford SR540 chopper. All the other measurements were performed under ambient atmosphere at room temperature.

3. RESULTS AND DISCUSSION

3.1. Photophysical Properties of $Cd_{0.75}Hg_{0.25}Te$ CQDs:PBTPV Layer. The absorption spectra of the films with different CQDs content are shown in Figure 1a. From the

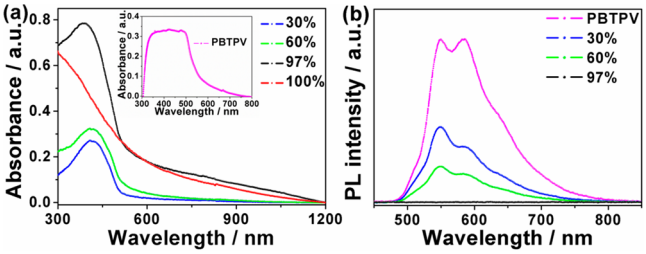

Figure 1. (a) The absorption spectra with different $Cd_{0.75}Hg_{0.25}Te$ CQDs content. Insert is absorption spectrum of PBTPV. (b) The PL emission quenching process with different $Cd_{0.75}Hg_{0.25}Te$ CQDs proportions with an excitation wavelength of 365 nm.

inset of Figure 1a, it is observed that the PBTPV film presents a broad absorption from 300 to 700 nm. In addition, the absorption of pure $Cd_{0.75}Hg_{0.25}Te$ CQDs is from 300 to 1200 nm (the red line in Figure 1a). Therefore, introducing $Cd_{0.75}Hg_{0.25}Te$ CQDs into PBTPV will further broaden the absorption spectrum of polymer from 700 to 1200 nm. In order to clearly show the contribution of $Cd_{0.75}Hg_{0.25}Te$ CQDs to the absorption, Figure S1 shows the magnification of the absorption spectra of pure polymer PBTPV and the blend films in the range of 700−1200 nm. It is observed that there exists gradual enhancement of absorption for the blend film with increasing the content of $Cd_{0.75}Hg_{0.25}Te$ CQDs from 30% to 60%. Especially, an abrupt increase in the absorption spectrum is shown when the $Cd_{0.75}Hg_{0.25}Te$ CQDs content increases to 97%. However, the polymer does not show any absorption in the range of 770−1200 nm. Therefore, the absorption spectrum of the blend film in the range of 770−1200 nm is only contributed by $Cd_{0.75}Hg_{0.25}Te$ CQDs. It is clearly observed that the absorption spectra of the blend film in Figure 1a show the peak characteristics of both PBTPV and $Cd_{0.75}Hg_{0.25}Te$ CQDs from UV to 1200 nm. In addition, Figure S2 gives the change of extinction coefficients with the wavelength. It is observed the extinction coefficients of PBTPV, $Cd_{0.75}Hg_{0.25}Te$ CQDs, and their blend film are all in the order of 10^4 at given range of wavelength, implying their good absorption capability. These results indicate that the PBTPV:$Cd_{0.75}Hg_{0.25}Te$ HSC will have a broad response to sunlight, which is favorable to its improvement of PCE. Figure 1b presents the photoluminescence (PL) spectra of PBTPV and blend films which were excited at 365 nm. The PL emission at 586 and 550 nm is attributed to strong $\pi-\pi$ interacting chains and the weak interactions without $\pi-\pi$ scaffold of PBTPV film, respectively. The PL spectra of PBTPV are gradually quenched with increasing the content CQDs, indicating that electron transfer from polymer to CQD might have occurred.

Figure 2a shows the energy structure of the PBTPV:$Cd_{0.75}Hg_{0.25}Te$ HSC device. Relative to the vacuum

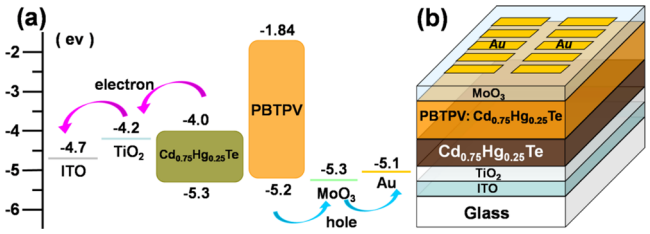

Figure 2. (a) The energy structure of the PBTPV:$Cd_{0.75}Hg_{0.25}Te$ HSC. (b) The device structure of the PBTPV:$Cd_{0.75}Hg_{0.25}Te$ HSC.

level, the highest occupied molecular orbital (HOMO) level of PBTPV is −5.2 eV, and the lowest unoccupied molecular orbital (LUMO) level is −1.84 eV. The conduction band of $Cd_{0.75}Hg_{0.25}Te$ CQDs is −4.0 eV, and the valence band is −5.3 eV[34,35] This energy band structure guarantees that the electrons can transfer from PBTPV to $Cd_{0.75}Hg_{0.25}Te$ CQDs. Therefore, it is easy to understand that the PL quenching of PBTPV results from the electron transfer from polymer to CQDs. The results indicate that the effective charge separate can occur in the device, which is an essential condition for high performance solar cells. Figure 2b shows the device structure where the single $Cd_{0.75}Hg_{0.25}Te$ CQDs modification layer was added to enhance the light absorption simultaneously as a hole block layer and electron transport layer.

3.2. Formation of the Interpenetrating Network. For an eligible photovoltaic device, an ideal electron transport path is another important factor to affect its performance. Therefore, a heat treatment process was carried out in order to form the interpenetrating network structure, which is favorable for the electron transport. Note that the PBTPV has an excellent thermal stability with the decomposition temperature of 550 °C (Figure S3), which guarantees its donor role under high temperature (300 °C). The absorption spectra of pure $Cd_{0.75}Hg_{0.25}Te$ CQDs annealed under different temperatures present absorption from 300 to 1200 nm and show little change (Figure S4). The formation process of interpenetrating network is presented in Scheme 2. In the active layer, the $Cd_{0.75}Hg_{0.25}Te$

Scheme 2. Photoactive Layer before and after Annealing and the Formation of the Interpenetrating Network Structure during Annealing

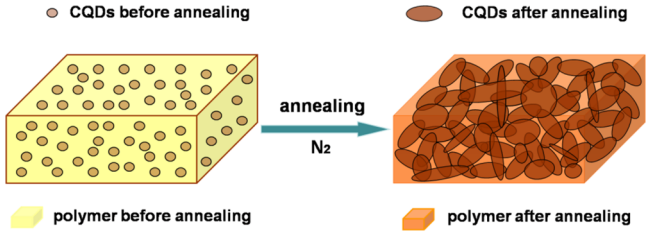

CQDs disperse in the polymer, and no interlinking exists until the occurrence of the annealing procedure. During the annealing, the content of surface ligands decreases, and the size of $Cd_{0.75}Hg_{0.25}Te$ CQDs becomes bigger. Under the limitation of the polymer chains, the $Cd_{0.75}Hg_{0.25}Te$ CQDs germinate and grow up with inhomogeneous size, which results in multiple hybrid heterojunctions (HHJs) at last. As a result, the interlinking of CQDs comes into being which provides an

dx.doi.org/10.1021/am501408v | ACS Appl. Mater. Interfaces 2014, 6, 8606−8612

unobstructed route for the charges carrier transportation. When the excitons are generated in the course of light absorption by PBTPV, they diffuse to HHJs where the consequent dissociation takes place. Consequently, the electrons transfer from PBTPV to $Cd_{0.75}Hg_{0.25}Te$ CQDs and then transport in the interpenetrating network.

Tapping mode of AFM is used to characterize the nanoscopic morphology of the blend film which directly monitors the formation process of the interpenetrating network. From Figure 3a/d, the blend film under 200 °C

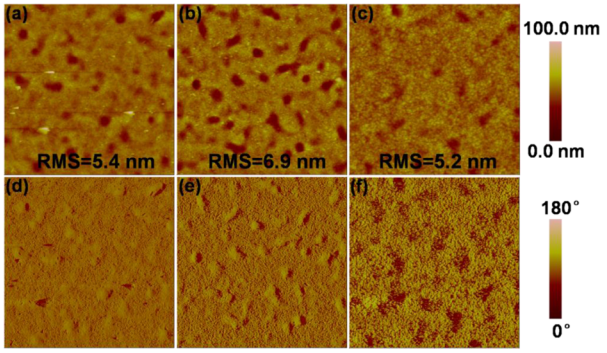

Figure 3. AFM (5 mm × 5 mm) topography (a–c) and the corresponding phase images (d–f) of the PBTPV:$Cd_{0.75}Hg_{0.25}Te$ active layer with various annealing temperature: (a and d) 200 °C, (b and e) 250 °C, (c and f) 300 °C. The active layer suffered from annealing for 60 min under N_2.

annealing shows a relative rough surface with a root-mean-square (RMS) roughness of 5.4 nm. However, it still looks smooth because of the small size of the $Cd_{0.75}Hg_{0.25}Te$ CQDs. Therefore, the CQDs are separately distributed in the blend film. With increasing the annealing temperature to 250 °C, the blend film apparently presents a two phase structure and the RMS roughness gets to 6.9 nm as shown in Figure 3b/e. Though a large aggregation region of the $Cd_{0.75}Hg_{0.25}Te$ CQDs appears, the blend film just establishes an unsound interpenetrating network structure. Accompanied with an apparent phase separation, the mature interpenetrating network forms when the annealing temperature increases to 300 °C. Moreover, the RMS roughness of the blend film decreases to 5.2 nm although larger CQDs formed as presented in Figure 3c/f. Such a structure will ensure the charge separation and smooth transport at the heterojunction.

TEM of the PBTPV:$Cd_{0.75}Hg_{0.25}Te$ active layer further confirms the formation of the interpenetrating network. From Figure 4a-b, it is observed that the size of the $Cd_{0.75}Hg_{0.25}Te$/CQDs composite is inhomogeneous with the average values of 10–20 nm under 200 and 250 °C heat treatment. When the temperature is increased to 300 °C, as shown in Figure 4c, an ideal $Cd_{0.75}Hg_{0.25}Te$ CQDs size of about 40 nm is obtained, which is of benefit to form an excellent interpenetrating network structure. Therefore, the domain size change is due to the growth of $Cd_{0.75}Hg_{0.25}Te$ CQDs from 3–5 nm before annealing to 10–40 nm after annealing at different temperatures until the formation of the interpenetrating network. Another important role of heat treatment is to remove the ligands on the surface of CQDs. As known, the existence of the ligands will severely hinder the transport of electrons, and, therefore, it is necessary to get rid of them as much as possible. Considering that 2-MA, the surface ligands on the CQDs, contains a characteristic N element, XPS analysis for the Cd 3d

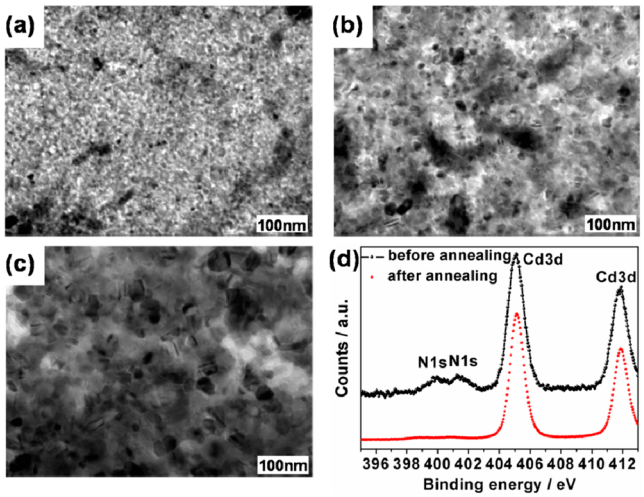

Figure 4. (a–c) TEM images of the PBTPV:$Cd_{0.75}Hg_{0.25}Te$ blend films at different annealing temperature (200, 250, and 300 °C). (d) XPS spectra of Cd 3d and N 1s in the blend film before and after annealing at 300 °C.

and N 1s is used to calculate the ligand content on the CQDs' surface after annealing as presented in Figure 4d. The obvious decrease of the surface ligands is detected, and the content reduces by 79.1% after annealing at 300 °C for 1 h. Therefore, most of the nonconductive ligands on the CQDs surfaces are removed during the annealing process. As a result, the annealed CQDs connect with each other, which is favorable for the electron transport. Moreover, it has been systematically investigated in our previous studies that the toxicity of $Cd_xHg_{1-x}Te$ CQDs mainly comes from the released Cd^{2+} and Hg^{2+}.[36] In this system, however, the aqueous-processed HSCs will not dissolve in water any more after annealing, which might avoid Cd^{2+} and Hg^{2+} entering into surroundings by rainwash.

The formation of the interpenetrating network is also confirmed by the measurement of carrier mobility at different temperatures. Electron-only carrier mobility was measured according to a similar method with a diode configuration of ITO/TiO_2/PBTPV:$Cd_{0.75}Hg_{0.25}Te$/Al using the space-charge-limited-current (SCLC) at low voltage which is calculated according to the Mott–Gurney equation

$$J = 9\varepsilon_0\varepsilon_r\mu V^2/8L^3$$

where ε_0 is the permittivity of free space (8.85×10^{-12} F m^{-1}), ε_r is the dielectric constant of $Cd_{0.75}Hg_{0.25}Te$ CQDs, μ is the electron mobility, V is the applied voltage, and L is the film thickness. By fitting the results to a space-charge-limited form, $J^{0.5}$ versus V_{appl} is plotted in Figure 5. The thickness of the blend film is about 80 nm detected by the Ambios Tech. XP-2 profilometer. The electron mobility of the $Cd_{0.75}Hg_{0.25}Te$ CQDs under different annealing temperature is calculated to be 1.4×10^{-5} cm^2 V^{-1} s^{-1} (200 °C), 8.3×10^{-5} cm^2 V^{-1} s^{-1} (250 °C), and 2.7×10^{-4} cm^2 V^{-1} s^{-1} (300 °C), respectively. It is observed that the electron mobility observably improves with increasing the annealing temperature, which means the formation of effective paths for the electron transport, namely, the increase of the annealing temperature results in the formation and perfection of the interpenetrating network. Moreover, the electron mobility of the $Cd_{0.75}Hg_{0.25}Te$ CQDs reaches 2.7×10^{-4} cm^2 V^{-1} s^{-1} under 300 °C, which is similar

dx.doi.org/10.1021/am501408v | ACS Appl. Mater. Interfaces 2014, 6, 8606–8612

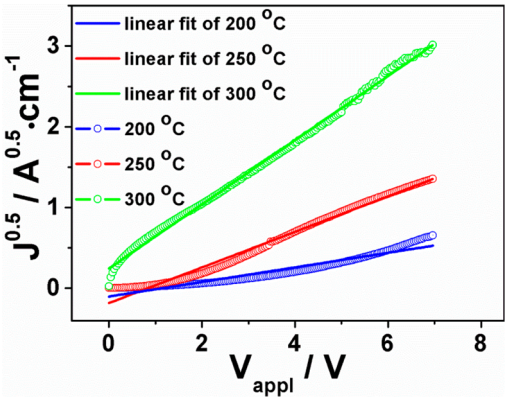

Figure 5. $J^{0.5}$ vs V_{appl} plots for the blend film under different annealing temperatures.

to the hole mobility of the PBTPV (5×10^{-4} cm^2 V^{-1} s^{-1}). This balanced electron/hole mobility ensures the effective charge-carrier transport, indicating a possible photovoltaic response.

3.3. Performance of the Devices. The devices with a structure of ITO/TiO_2/$Cd_{0.75}Hg_{0.25}Te$/PBTPV:$Cd_{0.75}Hg_{0.25}Te$/MoO_3/Au were fabricated via an aqueous-processed approach. Experiments to optimize the device performance are summarized in Table 1. As Figure 6a shows, due to the lack of interpenetrating network, a rather low PCE of about 0.0033% is detected under a low heat treatment temperature of 200 °C. When the temperature is increased to 250 °C, the interpenetrating network under growth period appears and thus results in better electron transport. Therefore, the shot-circuit current (J_{sc}) largely increases to 14.0 mA cm^{-2}. However, owning to the inmmature interpenetrating network, the open-circuit voltage (V_{oc}) of 0.26 V is still not satisfactory and leads to a low PCE of 1.1%. When the temperature is enhanced to 300 °C, a sturdy interpenetrating network structure is formed. Therefore, there is an observable improvement with a PCE of approximately 2.7%, which is the highest value for the NIR HSC fabricated in aqueous process by far. The J_{sc} (15.6 mA cm^{-2}), V_{oc} (0.4 V), and the highest PCE determine a fill factor (FF) of about 43.2%.

Table 1. Photovoltaic Performance under Different Preparation Conditions

conditions	J_{sc} (mA cm^{-2})	V_{oc} (V)	FF (%)	PCE (%)
200 °C/800 rpm	0.23	0.10	15.0	0.0033
250 °C/800 rpm	14.0	0.26	30.0	1.1
300 °C/800 rpm	15.6	0.40	43.2	2.7
300 °C/600 rpm	19.1	0.36	30.8	2.1

Figure S5 gives the J–V curve of the device ITO/TiO_2/PBTPV:$Cd_{0.75}Hg_{0.25}Te$/MoO_3/Au (namely, without the single $Cd_{0.75}Hg_{0.25}Te$ layer modification), which presents the J_{sc} (9.15 mA cm^{-2}), V_{oc} (0.38 V), FF (35.7%), and the PCE of 1.24% (Table S1). The J_{sc}, FF, and PCE are all lower than the one with the single $Cd_{0.75}Hg_{0.25}Te$ layer modification. Especially, the photocurrent increases 70% after introduction of this single CQD layer. This indicates that this layer plays an important role in this system because $Cd_{0.75}Hg_{0.25}Te$ CQDs are believed to act as light absorption simultaneously as a hole block and electron transport layer. In addition, rotating speed has an important effect on the performance of device, which determines the thickness of the film. The film thickness was adjusted by setting the rotating speed at 600 rpm on the $Cd_{0.75}Hg_{0.25}Te$ (about 50 nm) and PBTPV:$Cd_{0.75}Hg_{0.25}Te$ (about 100 nm) layers in order to obtain a thicker thickness which would lead to much more absorption. As we expected, the stronger absorption led to an extremely high promotion of J_{sc} (19.1 mA cm^{-2}). However, the surface roughness is generally inverse proportion to the rotating speed. Therefore, the PCE (2.1%) did not reach the peak value because of the relative rough surface under the low rotating speed (600 rpm), which resulted in a low FF of 30.8% (Table 1). Last but not least, the device structure is another important factor to the performance. For instance, the bilayer device of ITO/TiO_2/$Cd_{0.75}Hg_{0.25}Te$/PBTPV/MoO_3/Au was fabricated, which only shows PCE of 0.82% (Figure S5 and Table S1).

Figure 6b describes the external quantum efficiency measurement of the PBTPV:$Cd_{0.75}Hg_{0.25}Te$ HSC device (namely, the device with PCE of 2.7% in Table 1) annealed under the temperature of 300 °C. It is observed that this device has a wide response range in terms of the spectra covering from UV to 1100 nm, and the maximum value reaches 58.21% at 360 nm. By calculating, caused by the double-deck $Cd_{0.75}Hg_{0.25}Te$ CQDs, the contribution of the NIR spectra is great, and the ratio reaches 15.04% within the Herschel infrared region (780–1100 nm), which is 32% higher than the HSC device of PPV:$Cd_{0.75}Hg_{0.25}Te$. This result indicates that the PBTPV:$Cd_{0.75}Hg_{0.25}Te$ HSC device will present obviously an advantage in comparison with other HSC devices when applied in the cloudy region.

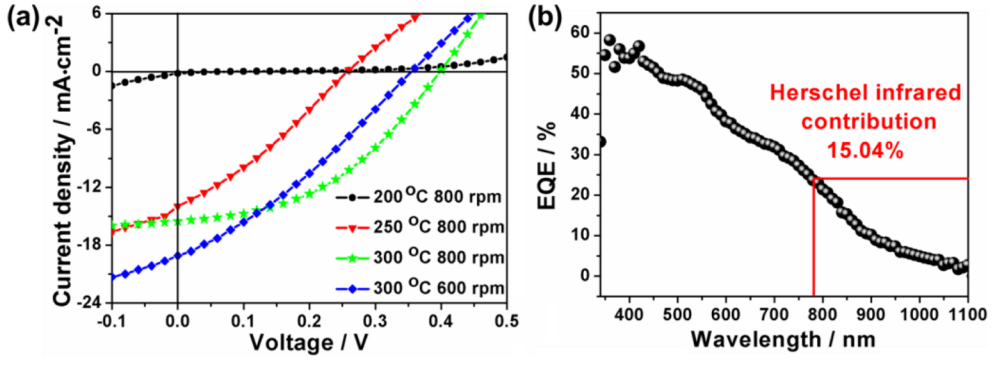

Figure 6. (a) J–V curves of the PBTPV:$Cd_{0.75}Hg_{0.25}Te$ HSC devices with different preparation conditions. (b) The EQE expression of the PBTPV:$Cd_{0.75}Hg_{0.25}Te$ HSC device after the heat treatment of 300 °C (the device with PCE of 2.7% in Table 1).

4. CONCLUSIONS

In summary, we successfully produced a sort of aqueous-processed PBTPV:$Cd_{0.75}Hg_{0.25}Te$ HSCs with an enormous Herschel infrared contribution. In line with the appreciable concept of green chemistry, we found an effective way to get an excellent PCE by altering the annealing temperature to obtain CQDs of diverse size with less ligands and simultaneously form an interpenetrating network as well as introducing the interfacial modification (single $Cd_{0.75}Hg_{0.25}Te$ CQDs layer) to enhance the absorbance. The PCE reached 2.7% under AM 1.5G illumination and conservatively estimated that the contribution of the NIR region attained 15.04% explored by the EQE measurement. To the best of our knowledge, this solar cell presents the highest PCE among HSCs based on $Cd_xHg_{1-x}Te$ CQDs and the highest NIR contribution among aqueous-processed HSCs, indicating the enormous potential of taking advantages of NIR energy in solar spectrum.

■ ASSOCIATED CONTENT

Ⓢ Supporting Information

The magnification of the absorption spectra of pure polymer PBTPV and the blend films in the range of 700−1200 nm, the change of extinction coefficients PBTPV, $Cd_{0.75}Hg_{0.25}Te$ CQDs and their blend film with the wavelength, TGA curve of the PBTPV precursor, the absorption spectrum of $Cd_{0.75}Hg_{0.25}Te$ CQDs under different temperatures, the *I-V* curve of the devices with different structures, and photovoltaic performance of different devices. This material is available free of charge via the Internet at http://pubs.acs.org.

■ AUTHOR INFORMATION

Corresponding Authors

*E-mail: sunhz335@nenu.edu.cn.

*Phone: +86-431-85099667. Fax: +86-431-85099667. E-mail: byangchem@jlu.edu.cn.

Notes

The authors declare no competing financial interest.

■ ACKNOWLEDGMENTS

This work was supported by the National Basic Research Development Program of China (2014CB643503), the Science Technology Program of Jilin Province (201201064 and 20130204025GX), and the NSFC (21221063 and 91123031).

■ REFERENCES

(1) Shah, A.; Torres, P.; Tscharner, R.; Wyrsch, N.; Keppner, H. Photovoltaic Technology: The Case for Thin-film Solar Cells. *Science* **1999**, *285*, 692−698.

(2) Saga, T. Advances in Crystalline Silicon Solar Cell Technology for Industrial Mass Production. *NPG Asia Mater.* **2010**, *2*, 96−102.

(3) Günes, S.; Neugebauer, H.; Sariciftci, N. S. Conjugated Polymer-based Organic Solar Cells. *Chem. Rev.* **2007**, *107*, 1324−1338.

(4) Habas, S. E.; Platt, H. A. S.; van Hest, M. F. A. M.; Ginley, D. S. Low-cost Inorganic Solar Cells: From Ink to Printed Device. *Chem. Rev.* **2010**, *110*, 6571−6594.

(5) Lee, M. M.; Teuscher, J.; Miyasaka, T.; Murakami, T. N.; Snaith, H. J. Efficient Hybrid Solar Cells Based on Meso-Superstructured Organometal Halide Perovskites. *Science* **2012**, *338*, 643−647.

(6) Guchhait, A.; Pal, A. J. Copper-Diffused $AgInS_2$ Ternary Nanocrystals in Hybrid Bulk-Heterojunction Solar Cells: Near-Infrared Active Nanophotovoltaics. *ACS Appl. Mater. Interfaces* **2013**, *5*, 4181−4189.

(7) Li, Y. Molecular Design of Photovoltaic Materials for Polymer Solar Cells: Toward Suitable Electronic Energy Levels and Broad Absorption. *Acc. Chem. Res.* **2012**, *45*, 723−733.

(8) Dong, Y.; Hu, X.; Duan, C.; Liu, P.; Liu, S.; Lan, L.; Chen, D.; Ying, L.; Su, S.; Gong, X.; Huang, F.; Cao, Y. A Series of New Medium-Band Gap Conjugated Polymers Based on Naphtho[1,2-c:5,6-c]bis(2-octyl-[1,2,3]triazole) for High-Performance Polymer Solar Cells. *Adv. Mater.* **2013**, *25*, 3683−3688.

(9) Hadipour, A.; de Boer, B.; Blom, P. W. M. Organic Tandem and Multi-junction Solar Cells. *Adv. Funct. Mater.* **2008**, *18*, 169−181.

(10) Li, W.; Hendriks, K. H.; Roelofs, W. S. C.; Kim, Y.; Wienk, M. M.; Janssen, R. A. J. Efficient Small Band Gap Polymer Solar Cells with High Fill Factors for 300 nm Thick Films. *Adv. Mater.* **2013**, *25*, 3182−3186.

(11) Seo, J. H.; Kim, D. H.; Kwon, S. H.; Song, M.; Choi, M. S.; Ryu, S. Y.; Lee, H. W.; Park, Y. C.; Kwon, J. D.; Nam, K. S.; Jeong, Y.; Kang, J. W.; Kim, C. S. High Efficiency Inorganic/Organic Hybrid Tandem Solar Cells. *Adv. Mater.* **2012**, *24*, 4523−4527.

(12) Mei, J.; Ogawa, K.; Kim, Y. G.; Heston, N. C.; Arenas, D. J.; Nasrollahi, Z.; McCarley, T. D.; Tanner, D. B.; Reynolds, J. R.; Schanze, K. S. Low-Band-Gap Platinum Acetylide Polymersas Active Materials for Organic Solar Cells. *ACS Appl. Mater. Interfaces* **2009**, *1*, 150−161.

(13) Kim, H.; Jeong, H.; An, T. K.; Park, C. E.; Yong, K. Hybrid-Type Quantum-Dot Cosensitized ZnO Nanowire Solar Cell with Enhanced Visible-Light Harvesting. *ACS Appl. Mater. Interfaces* **2013**, *5*, 268−275.

(14) Zhao, N.; Osedach, T. P.; Chang, L. Y.; Geyer, S. M.; Wanger, D.; Binda, M. T.; Arango, A. C.; Bawendi, M. G.; Bulovic, V. Colloidal PbS Quantum Dot Solar Cells with High Fill Factor. *ACS Nano* **2010**, *4*, 3743−3752.

(15) Kramer, I. J.; Sargent, E. H. Colloidal Quantum Dot Photovoltaics: A Path Forward. *ACS Nano* **2011**, *5*, 8506−8514.

(16) Baeten, L.; Conings, B.; Boyen, H. G.; D'Haen, J.; Hardy, A.; D'Olieslaeger, M.; Manca, J. V.; Bael, M. K. V. Towards Efficient Hybrid Solar Cells Based on Fully Polymer Infiltrated ZnO Nanorod Arrays. *Adv. Mater.* **2011**, *23*, 2802−2805.

(17) Yu, G.; Gao, J.; Hummelen, J. C.; Wudl, F.; Heeger, A. J. Polymer Photovoltaic Cells: Enhanced Efficiencies *via* a Network of Internal Donor-Acceptor Heterojunctions. *Science* **1995**, *270*, 1789−1791.

(18) Coffin, R. C.; Peet, J.; Rogers, J.; Bazan, G. C. Streamlined Microwave-Assisted Preparation of Narrow-Band Gap Conjugated Polymers for High-performance Bulk Heterojunction Solar Cells. *Nat. Chem.* **2009**, *1*, 657−661.

(19) Lek, J. Y.; Xi, L.; Kardynal, B. E.; Wong, L. H.; Lam, Y. M. Understanding the Effect of Surface Chemistry on Charge Generation and Transport in Poly (3-hexylthiophene)/CdSe Hybrid Solar Cells. *ACS Appl. Mater. Interfaces* **2011**, *3*, 287−292.

(20) Debnath, R.; Bakr, O.; Sargent, E. H. Solution-Processed Colloidal Quantum Dot Photovoltaics: A Perspective. *Energy Environ. Sci.* **2011**, *4*, 4870−4881.

(21) Son, H. J.; Wang, W.; Xu, T.; Liang, Y.; Wu, Y.; Li, G.; Yu, L. Synthesis of Fluorinated Polythienothiophene-*co*-benzodithiophenes and Effect of Fluorination on the Photovoltaic Properties. *J. Am. Chem.Soc.* **2011**, *133*, 1885−1894.

(22) Rakshit, T.; Mondal, S. P.; Manna, I.; Ray, S. K. CdS-Decorated ZnO Nanorod Heterostructures for Improved Hybrid Photovoltaic Devices. *ACS Appl. Mater. Interfaces* **2012**, *4*, 6085−6095.

(23) Xu, T.; Qiao, Q. Conjugated Polymer−Inorganic Semiconductor Hybrid Solar Cells. *Energy Environ. Sci.* **2011**, *4*, 2700−2720.

(24) Bardelang, D.; Zaman, M. B.; Moudrakovski, I. L.; Pawsey, S.; Margeson, J. C.; Wang, D.; Wu, X.; Ripmeester, J. A.; Ratcliffe, C. I.; Yu, K. Interfacing Supramolecular Gels and Quantum Dots with Ultrasound: Smart Photoluminescent Dipeptide Gels. *Adv. Mater.* **2008**, *20*, 4517−4520.

(25) Wang, R.; Ouyang, J.; Nikolaus, S.; Brestaz, L.; Zaman, M. B.; Wu, X.; Leek, D.; Ratcliffe, C. I.; Yu, K. Single-Sized Colloidal CdTe

Nanocrystals with Strong Band Gap Photoluminescence. *Chem. Commun.* **2009**, 962−964.
(26) Liu, Z.; Sun, Y.; Yuan, J.; Wei, H.; Huang, X.; Han, L.; Wang, W.; Wang, H.; Ma, W. High-Efficiency Hybrid Solar Cells Based on Polymer/PbS_xSe_{1-x}Nanocrystals Benefiting from Vertical Phase Segregation. *Adv. Mater.* **2013**, *25*, 5772−5778.
(27) Søndergaard, R.; Helgesen, M.; Jørgensen, M.; Krebs, F. C. Fabrication of Polymer Solar Cells Using Aqueous Processing for All Layers Including the Metal Back Electrode. *Adv. Energy Mater.* **2011**, *1*, 68−71.
(28) Wei, H.; Zhang, H.; Sun, H.; Yang, B. Preparation of Polymer-Nanocrystals Hybrid Solar Cells through Aqueous Approaches. *Nano Today* **2012**, *7*, 316−326.
(29) Andersen, T. R.; Larsen-Olsen, T. T.; Andreasen, B.; Böttiger, A. P. L.; Carlé, J. E.; Helgesen, M.; Bundgaard, E.; Norrman, K.; Andreasen, J. W.; Jørgensen, M.; Krebs, F. C. Aqueous Processing of Low-Band-Gap Polymer Solar Cells Using Roll-to-Roll Methods. *ACS Nano* **2011**, *5*, 4188−4196.
(30) Fan, Z.; Zhang, H.; Yu, W.; Xing, Z.; Wei, H.; Dong, Q.; Tian, W.; Yang, B. Aqueous-Solution-Processed Hybrid Solar Cells from Poly(1,4-naphthalenevinylene) and CdTe Nanocrystals. *ACS Appl. Mater. Interfaces* **2011**, *3*, 2919−2923.
(31) Yu, W.; Zhang, H.; Fan, Z.; Zhang, J.; Wei, H.; Zhou, D.; Xu, B.; Li, F.; Tian, W.; Yang, B. Efficient Polymer/Nanocrystal Hybrid Solar Cells Fabricated from Aqueous Materials. *Energy Environ. Sci.* **2011**, *4*, 2831−2834.
(32) Sun, H.; Zhang, H.; Ju, J.; Zhang, J.; Qian, G.; Wang, C.; Yang, B.; Wang, Z. One-step Synthesis of High-quality Gradient CdHgTe Nanocrystals: A Prerequisite to Prepare CdHgTe-Polymer Bulk Composites with Intense Near-Infrared Photoluminescence. *Chem. Mater.* **2008**, *20*, 6764−6769.
(33) Wei, H.; Zhang, H.; Sun, H.; Yu, W.; Liu, Y.; Chen, Z.; Cui, L.; Tian, W.; Yang, B. Aqueous-Solution-Processed PPV-$Cd_xHg_{1-x}Te$ Hybrid Solar Cells with a Significant Near-Infrared Contribution. *J. Mater. Chem.* **2012**, *22*, 17827−17832.
(34) Wei, H.; Zhang, H.; Jin, G.; Na, T.; Zhang, G.; Zhang, X.; Wang, Y.; Sun, H.; Tian, W.; Yang, B. Coordinatable and High Charge-Carrier-Mobility Water-Soluble Conjugated Copolymers for Effective Aqueous-Processed Polymer-Nanocrystal Hybrid Solar Cells and OFET Applications. *Adv. Funct. Mater.* **2013**, *23*, 4035−4042.
(35) Wei, H.; Sun, H.; Zhang, H.; Yu, W.; Zhai, F.; Fan, Z.; Tian, W.; Yang, B. Achieving High Open-circuit Voltage in the PPV-CdHgTe Bilayer Photovoltaic Devices on the Basis of the Heterojunction Interfacial Modification. *J. Mater. Chem.* **2012**, *22*, 9161−9165.
(36) Cai, W.; Jiang, L.; Yi, D.; Sun, H.; Wei, H.; Zhang, H.; Sun, H.; Yang, B. High Quality CdHgTe Nanocrystals with Strong Near-Infrared Emission: Relationship between Composition and Cytotoxic Effects. *Langmuir* **2013**, *29*, 4119−4127.